This is a repository copy of *Energy conservation during remeshing in the analysis of dynamic fracture*.

White Rose Research Online URL for this paper:
https://eprints.whiterose.ac.uk/148390/

Version: Accepted Version

Article:
Chen, L., Li, B. and Borst, R. (2019) Energy conservation during remeshing in the analysis of dynamic fracture. International Journal for Numerical Methods in Engineering, 120 (4). pp. 433-446. ISSN 0029-5981

https://doi.org/10.1002/nme.6142

This is the peer reviewed version of the following article: Chen, L, Li, B, Borst, R. Energy conservation during remeshing in the analysis of dynamic fracture. Int J Numer Methods Eng. 2019; 1– 14. https://doi.org/10.1002/nme.6142. This article may be used for non-commercial purposes in accordance with Wiley Terms and Conditions for Use of Self-Archived Versions.

Reuse
Items deposited in White Rose Research Online are protected by copyright, with all rights reserved unless indicated otherwise. They may be downloaded and/or printed for private study, or other acts as permitted by national copyright laws. The publisher or other rights holders may allow further reproduction and re-use of the full text version. This is indicated by the licence information on the White Rose Research Online record for the item.

Takedown
If you consider content in White Rose Research Online to be in breach of UK law, please notify us by emailing eprints@whiterose.ac.uk including the URL of the record and the reason for the withdrawal request.

eprints@whiterose.ac.uk
https://eprints.whiterose.ac.uk/

INTERNATIONAL JOURNAL FOR NUMERICAL METHODS IN ENGINEERING
Int. J. Numer. Meth. Engng 2018; **00**:1–16
Published online in Wiley Online Library (wileyonlinelibrary.com). DOI: 10.1002/nme

Energy conservation during remeshing in the analysis of dynamic fracture

Lin Chen[1], Bin Li[2], René de Borst[1*]

[1]*University of Sheffield, Department of Civil and Structural Engineering, Sheffield S1 3JD, UK*
[2]*Cornell University, Sibley School of Mechanical and Aerospace Engineering, Ithaca, NY 14853, USA*

SUMMARY

The analysis of (dynamic) fracture often requires multiple changes to the discretisation during crack propagation. The state vector from the previous time step must then be transferred to provide the initial values of the next time step. A novel methodology based on a least-squares fit is proposed for this mapping. The energy balance is taken as a constraint in the mapping, which results in a complete energy preservation. Apart from capturing the physics better, this also has advantages for numerical stability. To further improve the accuracy, Powell-Sabin B-splines, which are based on triangles, have been used for the discretisation. Since $\mathcal{C}^1$ continuity of the displacement field holds at crack tips for Powell-Sabin B-splines, the stresses at and around crack tips are captured much more accurately than when using elements with a standard Lagrangian interpolation, or with NURBS and T-splines. The versatility and accuracy of the approach to simulate dynamic crack propagation are assessed in two case studies, featuring mode-I and mixed-mode crack propagation. Copyright © 2018 John Wiley & Sons, Ltd.

Received . . .

KEY WORDS: dynamic fracture; Powell-Sabin B-splines; energy conservation; cohesive zone model; remeshing

1. INTRODUCTION

The analysis of dynamic crack propagation remains a challenging problem due to crack initiation, unstable propagation, branching, multiple crack interaction, coalescence and merging. To well understand these phenomena, numerical models, which for instance utilise cohesive crack models and phase field models, have been introduced in attempts to model crack nucleation, tortuous crack paths and micro-cracking in front of a main crack [1–4]. With dense meshes arbitrary crack paths can be captured fairly well [5].

The accurate calculation of the stress at the crack tip is a most important issue in the analysis of dynamic fracture [1, 2]. However, standard finite elements do not produce smooth stress field due to the $\mathcal{C}^0$ inter-element continuity [6]. The stresses are often inaccurate around crack tips unless extremely fine discretisations are used, and can therefore not be used readily in criteria for crack initiation and crack propagation. This tends to be even worse when using the extended finite element method [7–9]. For this reason, stresses are often averaged over finite domains, encompassing several elements [10]. Also, stress fields can be improved when enriching stress fields with higher-order terms [11], while crack tracking algorithms can also help to better simulate complex dynamic crack patterns, such as crack branching [12, 13]. Recently, phase-field models have been introduced to

*Correspondence to: R. de Borst, University of Sheffield, Department of Civil and Structural Engineering, Sheffield S1 3JD, UK. E-mail: r.deborst@sheffield.ac.uk

Copyright © 2018 John Wiley & Sons, Ltd.
Prepared using nmeauth.cls *[Version: 2016/03/02 v3.01]*

describe brittle fracture [14–16], allowing for a straightforward treatment of crack branching and merging [17].

Isogeometric analysis has also been introduced in the context of crack propagation analysis [18–23]. However, isogeometric analysis has some limitations to insert cracks at arbitrary locations as the initial mesh must be aligned sufficiently closely with the final crack path *a priori* [24]. Another disadvantage is that the higher-order continuity of the basis functions breaks down near crack tips and only $\mathcal{C}^0$-continuity remains, due to the insertion of $\mathcal{C}^0$ lines in order to shield the discontinuity due to the crack from the rest of the domain [24]. Since the splines basis functions satisfy the partition-of-unity property, an enrichment in the sense of the eXtended Finite Element method can also be used within isogeometric analysis, thus allowing for the propagation of discrete cracks independent from the underlying discretisation [25].

Herein we exploit Powell-Sabin B-splines for cohesive crack modelling [26]. Powell-Sabin B-splines are based on triangles. Direct crack insertion in the physical domain is possible due to the flexibility of triangles. Upon crack insertion, there may be elements with an unsuitable aspect ratio. Remeshing the domain around the crack tip is then required, which can be carried out fairly easy for triangular elements. After remeshing, new Powell-Sabin B-spline functions are computed on the new triangles. The state vectors (displacement, velocity and acceleration) must also be transferred to provide initial values for the next time step. This is done by a novel methodology based on a least-squares fit. To preserve the energy during the transfer, the energy is taken as a constraint in the mapping.

It is emphasised that for Powell-Sabin B-splines, different from NURBS and T-splines, the higher-order ($\mathcal{C}^1$) continuity is preserved at the crack tip, leading to continuous stress field around and at the crack tip [27, 28]. For this reason, the stresses are much more accurate and can directly be used in the crack initiation criterion. To facilitate the implementation Bézier extraction has been used, just as with NURBS and T-splines, and standard finite element data structures could therefore be exploited [29].

In this paper we first give a concise summary of the governing equations for the bulk and the crack interface. The cohesive zone model, the strong and the weak forms of equilibrium equation as well as the construction of Powell-Sabin B-splines are reviewed. We revisit the algorithm in [30] to insert a new crack segment, including the algorithm for remeshing after a crack insertion in Section 3. The state vector update after a crack insertion is discussed in Section 4, where emphasis is placed on energy conservation in dynamic fracture. Some numerical studies are illustrated in Section 5.

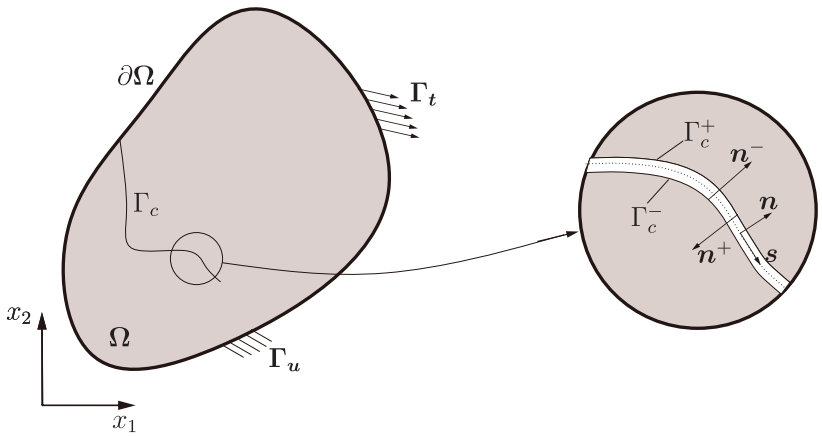

Figure 1. A solid body $\boldsymbol{\Omega}$ with an internal discontinuity Γ_c. Γ_c is an interface boundary with positive and negative sides, Γ_c^+ and Γ_c^-, respectively.

Copyright © 2018 John Wiley & Sons, Ltd.
Prepared using nmeauth.cls

DOI: 10.1002/nme

2. WEAK FORMULATION AND DISCRETISATION

In a discrete model a crack is considered as an interface Γ_c in the physical domain Ω, see Figure 1. Tractions on Γ_c are related to the crack opening and crack sliding. Infinitesimal deformations and linear elastic material behaviour have been assumed.

2.1. Cohesive zone model

The essence of the cohesive zone model is the relation between the tractions $\mathbf{t}_d$ acting on Γ_c and the displacement jump $[\![\boldsymbol{v}]\!]$ across it:

$$\mathbf{t}_d = \mathbf{t}_d\left([\![\boldsymbol{v}]\!]\right) = \{t_s,\ t_n\}^{\mathrm{T}}, \tag{1}$$

with $\mathbf{t}_d$ and $[\![\boldsymbol{v}]\!]$ defined in the local coordinate system $(s,\ n)$, see Figure 1. The tractions and relative displacements in the local coordinate system are related to the tractions $\mathbf{t}$ and the crack opening $[\![\mathbf{u}]\!]$ in the global coordinate system $(x_1,\ x_2)$ via a standard transformation:

$$[\![\boldsymbol{v}]\!] = \{[\![v_n]\!],\ [\![v_s]\!]\}^{\mathrm{T}} = \mathbf{R}\,[\![\mathbf{u}]\!] = \mathbf{R}\,\{[\![u_{x_1}]\!],\ [\![u_{x_2}]\!]\}^{\mathrm{T}}, \qquad \mathbf{t} = \mathbf{R}^{\mathrm{T}}\mathbf{t}_d, \tag{2}$$

with $\mathbf{R}$ as the rotation matrix [19].

In current study, an exponential decohesion formulation has been used to describe the traction–crack-opening relation [10]:

$$\begin{cases} t_n = t_u \exp\left(-\dfrac{t_u}{\mathcal{G}_c}\kappa\right) \\ t_s = d_{\text{int}} \exp\left(h_s\kappa\right)[\![v_s]\!] \end{cases} \tag{3}$$

where t_u is the fracture strength, $\mathcal{G}_c$ denotes the fracture energy, d_{int} represents the initial crack shear stiffness (when $\kappa = 0$), and $h_s = \ln\left(d_{\kappa=1.0}/d_{\text{int}}\right)$ governs the degradation of the shear stiffness. To prevent unphysical healing of the crack, a history parameter κ enters through a loading function $f = f([\![v_n]\!], [\![v_s]\!], \kappa)$, subject to the Kuhn-Tucker conditions [18]:

$$f \leqslant 0, , \qquad \dot{\kappa} \geqslant 0, \qquad \dot{\kappa} f = 0. \tag{4}$$

In case of unloading ($f < 0$), the tractions are obtained from a secant relation. To avoid interpenetration, a penalty stiffness $k_p = 10^5$ MPa/mm is specified in the normal direction.

2.2. Strong form and weak form

The strong form of linear momentum equation reads:

$$\nabla \cdot \boldsymbol{\sigma} - \rho\ddot{\mathbf{u}} = \mathbf{0} \qquad \text{on} \qquad \Omega \tag{5}$$

subject to the boundary conditions:

$$\begin{cases} \mathbf{u} = \hat{\mathbf{u}} & \text{on} \quad \Gamma_u \\ \boldsymbol{\sigma}\cdot\mathbf{n} = \hat{\mathbf{t}} & \text{on} \quad \Gamma_t \\ \boldsymbol{\sigma}\cdot\mathbf{n} = \mathbf{t}\left([\![\mathbf{u}]\!]\right) & \text{on} \quad \Gamma_c \end{cases}, \tag{6}$$

in which $\hat{\mathbf{u}}$ and $\hat{\mathbf{t}}$ represent prescribed displacements and tractions, respectively. ρ is the mass density, $\ddot{\mathbf{u}}$ denotes the acceleration vector, and a superimposed dot denotes a time derivative. $\mathbf{n}$ refers to the normal vector at the boundary. The Cauchy stress tensor $\boldsymbol{\sigma}$ relates to the infinitesimal strain $\boldsymbol{\varepsilon}$ as

$$\boldsymbol{\sigma} = \mathbf{D} : \boldsymbol{\varepsilon}, \tag{7}$$

where $\mathbf{D}$ is the fourth-order elastic stiffness tensor.

To solve the equilibrium Equation (5), it is cast in a weak form:

$$\delta W_{\text{int}} + \delta W_{\text{coh}} + \delta W_{\text{kin}} = \delta W_{\text{ext}}, \tag{8}$$

Copyright © 2018 John Wiley & Sons, Ltd.
Prepared using nmeauth.cls

DOI: 10.1002/nme

with

$$\begin{aligned} \delta W_{\text{int}} &= \int_{\Omega} \delta\boldsymbol{\varepsilon} : \boldsymbol{\sigma} \mathrm{d}\Omega \qquad \delta W_{\text{coh}} = \int_{\Gamma_c} \delta \left[\!\left[\mathbf{u}\right]\!\right] \cdot \mathbf{t} \left(\left[\!\left[\mathbf{u}\right]\!\right]\right) \mathrm{d}\Gamma \\ \delta W_{\text{kin}} &= \int_{\Omega} \delta\mathbf{u} \cdot \rho\ddot{\mathbf{u}} \mathrm{d}\Omega \qquad \delta W_{\text{ext}} = \int_{\Gamma_t} \delta\mathbf{u} \cdot \hat{\mathbf{t}} \mathrm{d}\Gamma \qquad \forall \delta\mathbf{u} \in \nu_0 \end{aligned} \tag{9}$$

where δ denotes the variation of a quantity, W_{int} designates the internal work, W_{coh} represents the work performed by the cohesive tractions on the crack surface Γ_c, W_{kin} is the kinetic energy, and W_{ext} is the work done by the externally applied loads. $\delta\boldsymbol{\varepsilon}$, $\delta\mathbf{u}$ and $\delta\left[\!\left[\mathbf{u}\right]\!\right]$ are the virtual strain, the virtual displacement and the virtual relative displacement fields, respectively, while $\nu_0 = \left\{\boldsymbol{v} : v_i \in H^1\left(\Omega\right), v_i|\,\Gamma_u = 0\right\}$, H^1 being the first-order Sobolev space.

To discretise Equation (8), Powell-Sabin B-splines are employed. They describe the geometry and interpolate the displacement field $\mathbf{u}$ in an isoparametric sense:

$$\mathbf{x} = \sum_{k=1}^{N_v} \sum_{j=1}^{3} N_k^j \boldsymbol{X}_k^j \qquad\qquad \mathbf{u} = \sum_{k=1}^{N_v} \sum_{j=1}^{3} N_k^j \boldsymbol{U}_k^j, \tag{10}$$

where $\boldsymbol{X}_k^j$ represent the coordinates of the corners $\boldsymbol{Q}_k^j$ of the Powell-Sabin triangles. $\boldsymbol{U}_k^j$ denotes the degrees of freedom at $\boldsymbol{Q}_k^j$ and N_v is the total number of vertices. The indices $j = 1, 2, 3$ imply that three Powell-Sabin B-splines are defined on each vertex k.

Inserting the kinematic small-strain relation into the weak form, Equation (8), yields the usual set of non-linear equations:

$$\mathbf{f}_{\text{kin}}\left(\mathbf{u}\right) + \mathbf{f}_{\text{int}}\left(\mathbf{u}\right) = \mathbf{f}_{\text{ext}}, \tag{11}$$

with

$$\begin{cases} \mathbf{f}_{\text{kin}}\left(\mathbf{u}\right) = \int_{\Omega} \rho\mathbf{N}^{\mathrm{T}}\ddot{\mathbf{u}} \mathrm{d}\Omega \\ \mathbf{f}_{\text{int}}\left(\mathbf{u}\right) = \int_{\Omega} \mathbf{B}^{\mathrm{T}}\boldsymbol{\sigma} \mathrm{d}\Omega + \int_{\Gamma_c} \mathbf{H}^{\mathrm{T}}\mathbf{t}\left(\left[\!\left[\mathbf{u}\right]\!\right]\right) \mathrm{d}\Gamma \\ \mathbf{f}_{\text{ext}} = \int_{\Gamma_t} \mathbf{N}^{\mathrm{T}}\hat{\mathbf{t}} \mathrm{d}\Gamma. \end{cases} \tag{12}$$

The matrices $\mathbf{N}$, $\mathbf{B}$ and $\mathbf{H}$ contain the shape functions, their derivatives, and the relative displacements, respectively [22]. Substituting the Powell-Sabin approximation, Equation (10), in Equation (12) yields the global system of equations:

$$\mathbf{M}\ddot{\mathbf{U}} + \mathbf{K}\mathbf{U} = \mathbf{f}_{\text{ext}}, \tag{13}$$

where $\mathbf{M}$ and $\mathbf{K}$ are the mass matrix and the stiffness matrix, respectively. The stiffness matrix $\mathbf{K}$ is additively decomposed into a contribution due to the bulk elements $\mathbf{K}_b$, and a contribution due to the cohesive crack interface, $\mathbf{K}_c$. The Newmark-β method is used for the time integration [31]. A Newton-Raphson method is used to attain equilibrium within each time step.

2.3. *Powell-Sabin B-splines*

We now give a succinct description of Powell-Sabin B-splines, while an in-depth elaboration can be found in Ref. [29]. A triangulation $\mathcal{T}$ is considered, which is denoted by the thick black lines in Figure 2(a). There are $e = 1, 2, \cdots, E$ triangles and N_v vertices defined over $\mathcal{T}$. The triangulation $\mathcal{T}$ can be generated by any package for standard triangular elements, such as Gmsh [32]. To construct Powell-Sabin B-splines, each triangle e of the triangulation $\mathcal{T}$ has to be split into six mini-triangles, see Figure 2(b). This results in the Powell-Sabin refinement $\mathcal{T}^*$. For each vertex k Powell-Sabin points are plotted in green as the vertex itself and points lying at the centre of the edges of $\mathcal{T}^*$. A Powell-Sabin triangle (in red), which contains all the Powell-Sabin points, is defined for each vertex k. Herein, we employ the algorithm of Ref. [33] to find the minimum area triangle which encloses

Copyright © 2018 John Wiley & Sons, Ltd.
Prepared using nmeauth.cls

DOI: 10.1002/nme

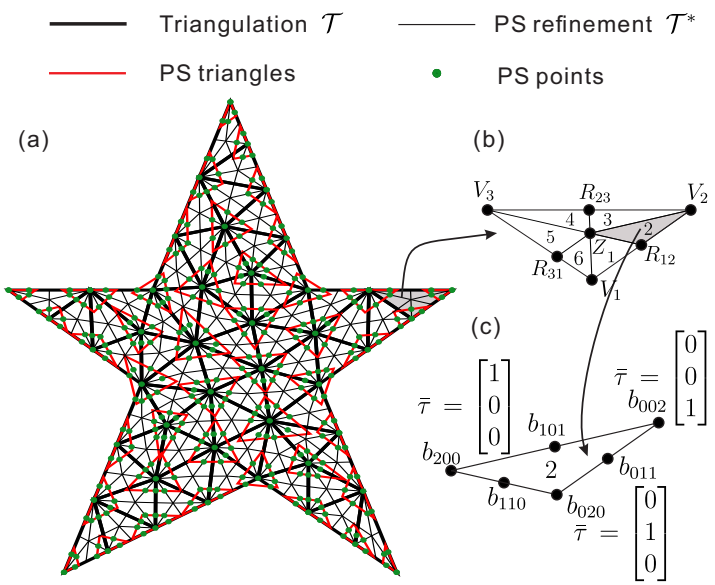

Figure 2. Example of a triangulation $\mathcal{T}$ (thick black lines), Powell-Sabin refinement $\mathcal{T}^*$ (thin black lines) of $\mathcal{T}$, Powell-Sabin triangles (red) and Powell-Sabin points (green). In (b) each triangle e is subdivided into six mini-triangles. In (c) each mini-triangle has a barycentric coordinate system $\bar{\tau}$.

the convex polygon defined by Powell-Sabin points. We further constrain the Powell-Sabin triangles on the boundary as follows: for an angle of $\gamma < 180°$ two sides of the Powell-Sabin triangle must be aligned with the two boundary edges, while for an angle of $\gamma = 180°$, one edge of the Powell-Sabin triangle must lie on the boundary. No restrictions are imposed on Powell-Sabin triangles at an internal discontinuity (crack interface).

Three Powell-Sabin B-splines N_k^j, $j = 1, 2, 3$, are defined on each vertex k with coordinates $\boldsymbol{V}_k = \left(x_1^k, x_2^k\right)$, i.e. one for each corner of the Powell-Sabin triangle of vertex k. For any vertex $\boldsymbol{V}_k \neq \boldsymbol{V}_l$ we have:

$$N_k^j\left(\boldsymbol{V}_l\right) = 0, \qquad \frac{\partial}{\partial x_1} N_k^j\left(\boldsymbol{V}_l\right) = 0, \qquad \frac{\partial}{\partial x_2} N_k^j\left(\boldsymbol{V}_l\right) = 0, \tag{14}$$

and otherwise

$$N_k^j\left(\boldsymbol{V}_k\right) = \alpha_k^j, \qquad \frac{\partial}{\partial x_1} N_k^j\left(\boldsymbol{V}_k\right) = \beta_k^j, \qquad \frac{\partial}{\partial x_2} N_k^j\left(\boldsymbol{V}_k\right) = \gamma_k^j, \tag{15}$$

with

$$\sum_{j=1}^{3} \alpha_k^j = 1, \qquad \sum_{j=1}^{3} \beta_k^j = 0, \qquad \sum_{j=1}^{3} \gamma_k^j = 0. \tag{16}$$

The coefficients α_k^j, β_k^j and γ_k^j are subsequently obtained by solving the linear system

$$\begin{bmatrix} \alpha_k^1 & \alpha_k^2 & \alpha_k^3 \\ \beta_k^1 & \beta_k^2 & \beta_k^3 \\ \gamma_k^1 & \gamma_k^2 & \gamma_k^3 \end{bmatrix} \begin{bmatrix} x_1^{k,1} & x_2^{k,1} & 1 \\ x_1^{k,2} & x_2^{k,2} & 1 \\ x_1^{k,3} & x_2^{k,3} & 1 \end{bmatrix} = \begin{bmatrix} x_1^k & x_2^k & 1 \\ 1 & 0 & 0 \\ 0 & 1 & 0 \end{bmatrix}, \tag{17}$$

in which $\boldsymbol{Q}_k^j = \left(x_1^{k,j}, x_2^{k,j}\right)$ are the coordinates of the corner of the Powell-Sabin triangles which are associated with vertex k. With the coefficients α_k^j, β_k^j and γ_k^j, the Bézier ordinates of each mini-triangle n in element e can be computed. The Bézier ordinates are assembled in the Bézier extraction operator $\boldsymbol{C}_n^e$, which allows for an efficient computation of the basis functions and their derivatives. We denote the Powell-Sabin B-splines associated with mini-triangle n in element e by $\boldsymbol{N}_n^e$. Then,

Copyright © 2018 John Wiley & Sons, Ltd.
Prepared using nmeauth.cls

DOI: 10.1002/nme

$\boldsymbol{N}_n^e$ are computed from:

$$\boldsymbol{N}_n^e = \boldsymbol{C}_n^e \boldsymbol{B}, \tag{18}$$

with the six Bernstein polynomials, contained in the vector $\boldsymbol{B}$ [29].

Extension to three-dimensional crack propagation is problematic when using Powell-Sabin B-splines. No procedure is yet available to define them on arbitrary tetrahedral meshes because of certain constraints with neighbouring tetrahedrons [41, 42], and they currently only work for structured meshes.

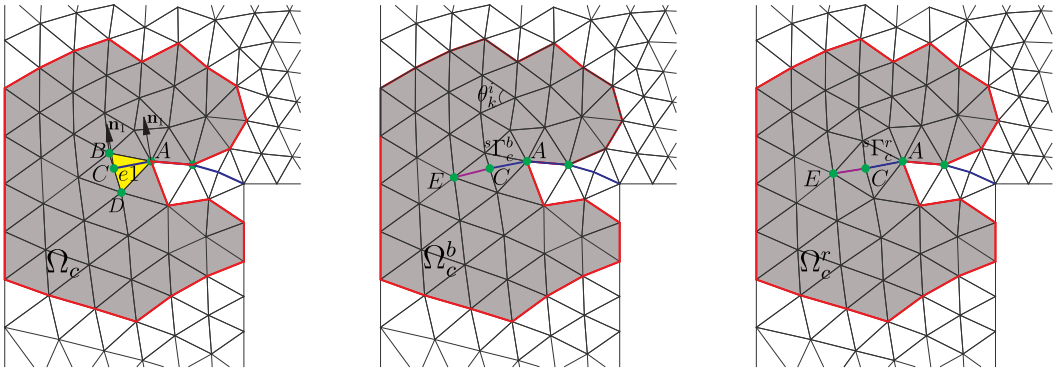

(a) crack propagation (b) element adjustment (c) remeshing

Figure 3. Mesh before and after remeshing. The blue solid curve denotes the crack interface Γ_c. Point A gives the old crack tip, while point C denotes the new crack tip. Segment AC represents the new crack interface. Ω_c is the mesh before element adjustment. Ω_c^b and Ω_c^r denote the meshes before and after remeshing Ω_c.

3. ADAPTIVE ANALYSIS FOR COHESIVE CRACK GROWTH

Due to the $\mathcal{C}^1$ continuity of the Powell-Sabin B-splines at the crack tip, e.g. point A in Figure 3(a), crack initiation can be assessed by directly comparing the major principal stress σ_1 at A with the tensile strength t_u. If $\sigma_1 > t_u$, the crack is allowed to propagate. The crack is then extended through the entire element $e1$, see Figure 3(a). The new crack tip is therefore at C. Due to lack of information about the possible curvature of the crack, it is introduced as a straight line within the element [34, 35]. An accurate computation of the normal vector to the crack, $\mathbf{n}_1$, is essential for the proper location of the new crack tip, see Figure 3(a). Indeed, considering the $\mathcal{C}^1$-continuity of the Powell-Sabin B-splines, one can, in principle, directly evaluate $\mathbf{n}_1$ from the stress tensor at the previous location of the crack tip. However, to further improve the quality of the prediction of the *direction* of crack propagation we average the stress tensor over a small, but finite domain [10].

Upon insertion of a new crack segment, element $e1$ is divided into two triangles, see Figure 3(a). The element next to the new crack tip has four vertices, which is not allowed for Powell-Sabin B-splines [26]. Thus, remeshing is needed for the domain with the new crack tip. We consider two cases, depending on the ratio $\zeta = |BC| \,/\, |CD|$, where $|BC|$ and $|CD|$ are lengths of line segments BC and CD, respectively, see Figure 3(a):

Case 1: If ζ is small or is large, $\zeta < 0.5$ or $\zeta > 2$, point C will be too close to either point B or to point D. To remedy this, we merge point C with the closest point between points B and D. Then, we remesh the domain with the merged crack tip.

Case 2: If the ratio ζ is moderate, $0.5 \leq \zeta \leq 2$, point C will be in the central part between points B and D. We retain both triangles after crack insertion and divide the element next to the new crack tip into two triangles, see Figure 3(b). Afterwards, the domain with the new crack tip is remeshed.

Remeshing is carried out only for elements near the crack tip. For example, only the grey area Ω_c^b inside the red polygon of Figure 3(b) is remeshed, and the vertices on and outside the red polygon

Copyright © 2018 John Wiley & Sons, Ltd.
Prepared using nmeauth.cls

DOI: 10.1002/nme

and the crack tips will not change location. Here, Ω_c^b denotes the mesh after element adjustment with the crack segment insertion. The area Ω_c^b is set as follows: it starts at the element with the newly inserted crack segment, i.e. the yellow element $e1$ in Figure 3(a), and then a radial marching is done until three elements have been crossed in all directions, see Figure 3(b). Next, we exclude the elements along one side of the crack interface. In Figure 3(b) this applies to the elements along the lower side of the crack interface.

The remeshing then proceeds by requiring that the minimum interior angle θ^1_{min} be maximised of all triangles inside Ω_c^b:

$$\begin{array}{ll} \max & \theta^1_{\text{min}} \\ \text{subject to:} & \theta^i_k \geq \theta^1_{\text{min}} \\ & \theta^1_{\text{min}} \geq \pi/6 \end{array} , \tag{19}$$

where θ^i_k is the i^{th} interior angle ($i = 1, 2, 3$) of triangle k, see Figure 3(b). After obtaining the minimum interior angle θ^1_{min}, we can further remesh the domain by using Equation (19) to maximise the second minimum interior angle θ^2_{min} of all triangles inside Ω_c^b. This procedure can be repeated until all interior angles have attained a maximum value. Figure 3(c) shows the mesh Ω_c^r after remeshing of Ω_c^b.

4. STATE VECTOR UPDATE AFTER CRACK INSERTION

During crack propagation new elements and vertices are introduced as a consequence of inserting new crack segments. Moreover, after crack insertion, remeshing of Ω_c is required to enforce elements with suitable aspect ratio. Accordingly, Powell-Sabin B-spline functions must be computed on the remeshed area Ω_c^r. Here, the mesh before remeshing is denoted as Ω_c^b, while the mesh after remeshing is represented as Ω_c^r.

For non-linear problems, remeshing also requires a transfer of the state vectors like the displacement, the velocity and the acceleration from the previous time t in order to provide the initial values at the new time $t + \Delta t$. We firstly map the discrete displacements ${}^t\mathbf{U}_b$ from the previous time step t onto ${}^{t+\Delta t}_0\mathbf{U}_r$, which holds at time $t + \Delta t$. Next we define $\mathbf{N}_b$ and $\mathbf{N}_r$ as the Powell-Sabin B-spline functions associated with the meshes before, i.e. Ω_c^b, and after remeshing Ω_c, i.e. Ω_c^r. Now, a least-squares fit is employed to carry out the mapping of ${}^t\mathbf{U}_b$ onto ${}^{t+\Delta t}_0\mathbf{U}_r$. This is achieved by minimising:

$$\psi = \int_{\Omega_c} \left\| {}^{t+\Delta t}_0\mathbf{u}_r - {}^t\mathbf{u}_b \right\| \mathrm{d}\Omega = \int_{\Omega_c} \left\| {}^{t+\Delta t}\mathbf{N}_r \; {}^{t+\Delta t}_0\mathbf{U}_r - {}^t\mathbf{N}_b \; {}^t\mathbf{U}_b \right\| \mathrm{d}\Omega \tag{20}$$

in which $\mathbf{u}_b$ and $\mathbf{u}_r$ are displacement fields before and after remeshing, respectively.

In general, the set up of the Powell-Sabin B-spline functions after crack insertion does not guarantee energy conservation between the meshes Ω_c^b and Ω_c^r. To minimise the difference of the energy between Ω_c^b and Ω_c^r, the minimisation of ψ in Equation (20) is achieved by enforcing the energy constraint:

$$W^b_{\text{int}} + W^b_{\text{coh}} = W^r_{\text{int}} + W^r_{\text{coh}} \tag{21}$$

which can be re-expressed as, cf. Equation (9):

$$\int_{\Omega_c^b} \boldsymbol{\varepsilon} : \boldsymbol{\sigma} \mathrm{d}\Omega + \int_{{}^s\Gamma_c^b} [\![\mathbf{u}]\!] \cdot \mathbf{t} \left([\![\mathbf{u}]\!] \right) \mathrm{d}\Gamma = \int_{\Omega_c^r} \boldsymbol{\varepsilon} : \boldsymbol{\sigma} \mathrm{d}\Omega + \int_{{}^s\Gamma_c^r} [\![\mathbf{u}]\!] \cdot \mathbf{t} \left([\![\mathbf{u}]\!] \right) \mathrm{d}\Gamma \tag{22}$$

where ${}^s\Gamma_c^b$ and ${}^s\Gamma_c^r$ are the newly inserted crack segment in Ω_c^b and Ω_c^r, respectively. In Figure 3(c), ${}^s\Gamma_c^b$ and ${}^s\Gamma_c^r$ are the line segment AC.

Before crack insertion, e.g. element $e1$ in Figure 3(a), there is no crack opening in $e1$. Thus, we must prevent crack opening in element $e1$ after inserting a new crack segment. On the line AC in

Copyright © 2018 John Wiley & Sons, Ltd.
Prepared using nmeauth.cls

DOI: 10.1002/nme

Figure 3(c) we must have:

$$ {}^{t+\Delta t}_{0}\mathbf{u}_r - {}^{t}\mathbf{u}_b = \mathbf{0} \qquad \text{on} \qquad {}^{s}\Gamma_c^r. \tag{23} $$

This is a general formulation for the crack segment AC. In the computation certain representative points should be chosen. Here, we have chosen the value at the integration points to satisfy this equation:

$$ {}^{t+\Delta t}\mathbf{N}_r \, {}^{t+\Delta t}_{0}\mathbf{U}_r - {}^{t}\mathbf{N}_b \, {}^{t}\mathbf{U}_b = \mathbf{0} \qquad \text{at integration points on} \qquad {}^{s}\Gamma_c^r \tag{24} $$

Three integration points are chosen along ${}^{s}\Gamma_c^r$. This guarantees satisfaction of Equation (23) exactly due to the $\mathcal{C}^1$ continuity of Powell-Sabin B-splines.

In sum, for a proper transfer of the displacements ${}^{t}\mathbf{U}_b$ at time t to ${}^{t+\Delta t}_{0}\mathbf{U}_r$ at time $t+\Delta t$, one must solve the following optimisation problem:

$$ \text{min} \qquad \int_{\Omega_c} \left\| {}^{t+\Delta t}\mathbf{N}_r \, {}^{t+\Delta t}_{0}\mathbf{U}_r - {}^{t}\mathbf{N}_b \, {}^{t}\mathbf{U}_b \right\| \mathrm{d}\Omega, \tag{25a} $$

$$ \text{subject to:} \qquad \underbrace{W^b_{\text{int}} + W^b_{\text{coh}}}_{\text{on } \Omega_c^b} = \underbrace{W^r_{\text{int}} + W^r_{\text{coh}}}_{\text{on } \Omega_c^r} \tag{25b} $$

$$ {}^{t+\Delta t}\mathbf{N}_r \, {}^{t+\Delta t}_{0}\mathbf{U}_r - {}^{t}\mathbf{N}_b \, {}^{t}\mathbf{U}_b = \mathbf{0} \;\; \text{at integration points on} \;\; {}^{s}\Gamma_c^r $$

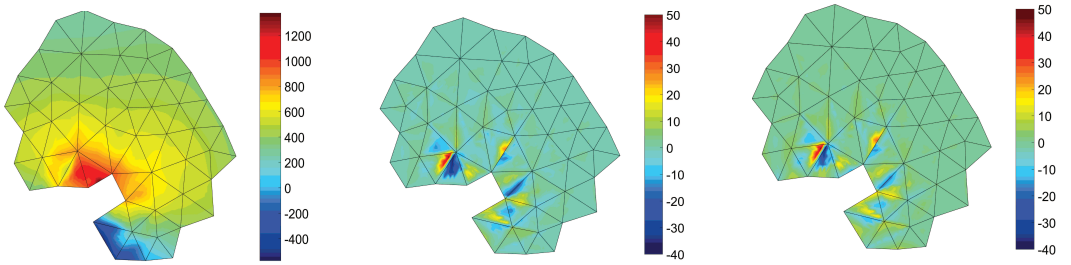

(a) "exact" σ_1 contour plot (b) error in σ_1 without constraint (c) error in σ_1 with constraint

Figure 4. The "exact" major principal stress σ_1 and error after remeshing. The "exact" solution refers to the stress in the mesh before the crack insertion. The error is given as the difference between the exact solution and the solution on the mesh after the crack insertion and remeshing. Figure (b) is the result from optimising Equation (25a) without constraint, Equation (25b); Figure (c) presents the result taking the constraint, Equation (25b), into account. The results shown here are from the problem in Section 5.2.

In principle, Equation (25a) can be minimised without constraining it by Equation (25b). This is the usual way to perform state vector transfer in the crack propagation analysis [30, 36]. In Figure 4 we compare the results of minimising Equation (25a) with and without constraint, i.e. Equation (25b). Qualitatively, the error contours are similar whether the constraint of Equation (25b) is taken into account or not. However, quantitatively differences arise. To quantify the error we therefore compute the relative error over the domain, which is defined by the L^2 error norm [37, 38]:

$$ \varepsilon = \frac{\|\sigma_1 - \bar{\sigma}_1\|_{L^2(\Omega_c^r)}}{\sqrt{\int_{\Omega_c} \sigma_1 \cdot \sigma_1 \, \mathrm{d}S}} = \frac{\sqrt{\int_{\Omega_c^r} (\sigma_1 - \bar{\sigma}_1) \cdot (\sigma_1 - \bar{\sigma}_1) \, \mathrm{d}S}}{\sqrt{\int_{\Omega_c} \sigma_1 \cdot \sigma_1 \, \mathrm{d}S}} \tag{26} $$

where σ_1 stands for the exact solution referred to the stress on the mesh Ω_c before the crack insertion, and $\bar{\sigma}_1$ denotes the solution after the crack insertion and remeshing.

The relative error ε in Figure 4(b) is 2.44%, while ε in Figure 4(c) is 1.32%, which is just a moderate difference. However, when checking the energy for both cases, the relative difference between the energies in Figure 4(a) and Figure 4(b) is 0.31152%, while that between the energies

Copyright © 2018 John Wiley & Sons, Ltd.
Prepared using nmeauth.cls

DOI: 10.1002/nme

of Figure 4(a) and Figure 4(c) is a computed zero, namely $0.409 \times 10^{-18}\%$. This is significant since energy preservation is of utmost importance for dynamic calculations in general, and for fracture propagation in particular, and much more important than the error committed in the displacements or even the stresses.

In the dynamic analysis of fracture, after remeshing Ω_c^b, we also need to transfer velocity fields ${}^t\dot{\mathbf{U}}_b$ from the previous time step t to provide initial values ${}_0^{t+\Delta t}\dot{\mathbf{U}}_r$ at time step $t+\Delta t$, which is achieved by an approach similar to that in Equations (25a) and (25b):

$$\text{min} \qquad \int_{\Omega_c} \left\| {}^{t+\Delta t}\mathbf{N}_r \; {}_0^{t+\Delta t}\dot{\mathbf{U}}_r - {}^t\mathbf{N}_b \; {}^t\dot{\mathbf{U}}_b \right\| \mathrm{d}\Omega, \tag{27a}$$

$$\text{subject to:} \qquad \underbrace{W_{\text{kin}}^b}_{\text{on } \Omega_c^b} - \underbrace{W_{\text{kin}}^r}_{\text{on } \Omega_c^r} = 0 \quad \Longrightarrow \quad \int_{\Omega_c^b} \rho \dot{\mathbf{u}}^{\mathrm{T}} \cdot \dot{\mathbf{u}} \mathrm{d}\Omega - \int_{\Omega_c^r} \rho \dot{\mathbf{u}}^{\mathrm{T}} \cdot \dot{\mathbf{u}} \mathrm{d}\Omega = 0 \tag{27b}$$

$$\text{,}$$

$${}^{t+\Delta t}\mathbf{N}_r \; {}_0^{t+\Delta t}\dot{\mathbf{U}}_r - {}^t\mathbf{N}_b \; {}^t\dot{\mathbf{U}}_b = \mathbf{0} \;\; \text{at integration points on} \;\; {}^s\Gamma_c^r$$

where W_{kin} is the kinetic energy. Here, the first equation in Equation (27b) will guarantee the conservation of kinetic energy in the velocity transfer. The second equation in Equation (27b) eliminates the velocity jump after the insertion of the crack segment ${}^s\Gamma_c^r$.

We have again compared the velocities after transfer with and without considering the constraint, Equation (27b). As expected, Figure 5 shows that the errors in both cases are similar in a qualitative sense. However, this no longer holds when examining the error quantitatively. For this, we have employed the relative error of the velocity, which is evaluated using the L^2 error norm. It is defined as in Equation (26), but σ_1 is replaced by the velocity in x direction, $\dot{u}_x$. The relative error ε for the results shown in Figure 5(b) is 1.44%, while ε for Figure 5(c) amounts to 0.68%. However, when examining the kinetic energy, much larger differences are again found: the relative difference between the kinetic energies in Figures 5(a) and 5(b) is 0.6953%, while that between Figures 5(a) and 5(c) is $0.759 \times 10^{-16}\%$, which is again a computed zero, so that the algorithm with constraint also fully preserves the kinetic energy, although it only halves the velocity components.

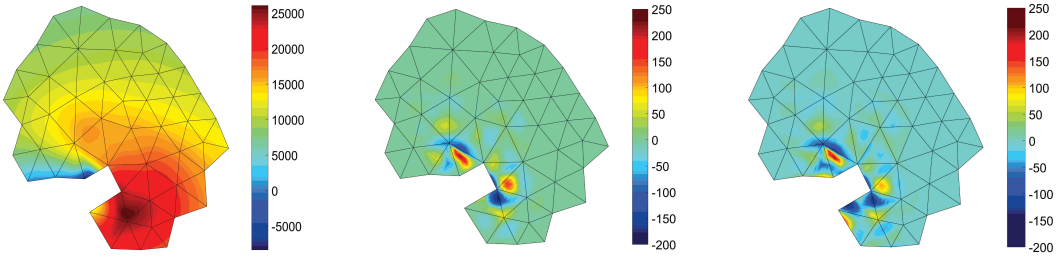

(a) "exact" $\dot{u}_x$ contour plot (b) error in $\dot{u}_x$ without constraint (c) error in $\dot{u}_x$ with constraint

Figure 5. "Exact" velocity component $\dot{u}_x$ and error after remeshing. The "exact" solution refers to the velocity before the crack insertion. The error is given as the difference between the exact solution and the solution after crack insertion and remeshing. Figure (b) gives the result when optimising Equation (27a) without constraint, Equation (27b), while Figure (c) presents the result with constraint, Equation (27b). The results shown here are from the problem in Section 5.2.

We have done the transfer of the acceleration ${}^t\ddot{\mathbf{U}}_b$ at time t to generate the initial values ${}_0^{t+\Delta t}\ddot{\mathbf{U}}_r$ at time $t+\Delta t$ in a similar way as in Equations (27a) and (27b):

$$\text{min} \qquad \int_{\Omega_c} \left\| {}^{t+\Delta t}\mathbf{N}_r \; {}_0^{t+\Delta t}\ddot{\mathbf{U}}_r - {}^t\mathbf{N}_b \; {}^t\ddot{\mathbf{U}}_b \right\| \mathrm{d}\Omega, \tag{28a}$$

$$\text{subject to:} \qquad \int_{\Omega_c^b} \rho \ddot{\mathbf{u}}^{\mathrm{T}} \cdot \ddot{\mathbf{u}} \mathrm{d}\Omega - \int_{\Omega_c^r} \rho \ddot{\mathbf{u}}^{\mathrm{T}} \cdot \ddot{\mathbf{u}} \mathrm{d}\Omega = 0 \tag{28b}$$

$$\text{.}$$

$${}^{t+\Delta t}\mathbf{N}_r \; {}_0^{t+\Delta t}\ddot{\mathbf{U}}_r - {}^t\mathbf{N}_b \; {}^t\ddot{\mathbf{U}}_b = \mathbf{0} \;\; \text{at integration points on} \;\; {}^s\Gamma_c^r$$

Copyright © 2018 John Wiley & Sons, Ltd.

Prepared using nmeauth.cls
DOI: 10.1002/nme

The first equation in Equation (28b) reads similar to the kinetic energy. The second equation in Equation (27b) excludes the acceleration jump after the insertion of the crack segment ${}^{s}\Gamma_c^{\tau}$. In Figure 6 we compare the acceleration after transfer with and without constraint. Qualitatively, the results are again similar, but quantitavely there are differences. To quantify the difference we use the relative error of the acceleration, which is defined similarly as in Equation (26) by replacing σ_1 by the acceleration in the x direction, $\ddot{u}_x$. The relative error ε without constraint, depicted in Figure 6(b), is 4.36%, while ε = 2.64% with constraint, see Figure 6(c). Although this difference is significant, the most important advantage of adding the constraint is the fact that energy is fully preserved during the mapping.

In addition to the benefit which taking the energy constraint into account has for energy preservation in analyses of dynamic fracture, it adds to the convergence behaviour of the equilibrium finding process. Indeed, there can be problems with convergence of the discrete non-linear set of equations when the constraint equation is not explicitly taken into account. Modest errors may accumulate, and ultimately lead to divergence of the Newton-Raphson procedure.

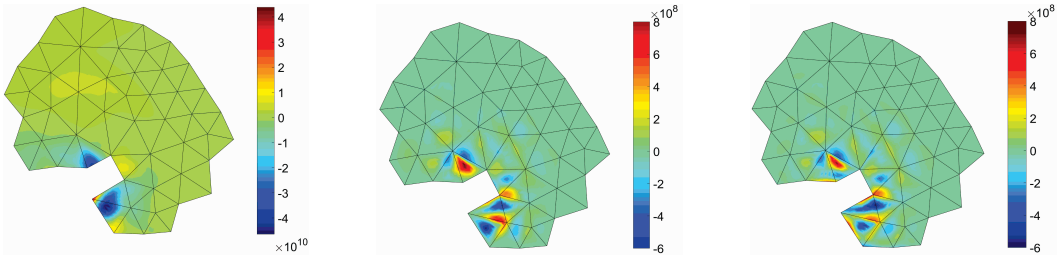

(a) "exact" $\ddot{u}_x$ contour plot (b) error in $\ddot{u}_x$ without constraint (c) error in $\ddot{u}_x$ with constraint

Figure 6. The "exact" acceleration in x-direction, $\ddot{u}_x$ and error after remeshing. The "exact" solution refers to the acceleration before crack insertion. The error is given as the difference between the exact solution and the solution after crack insertion and remeshing. Figure (b) is the result for optimising Equation (28a) without using the constraint, Equation (28b), while Figure (c) shows the result with constraint, Equation (28b). The results are from the problem in Section 5.2.

5. CASE STUDIES

We will now investigate two cases to assess the performance of the method. The first case concerns the analysis of model-I crack propagation in a specimen which is loaded at a constant velocity. The second case deals with a case where the crack shows a sharp kink with the initial notch. In both cases linear, isotropic elasticity is assumed for the bulk material. Mesh objectivity has been verified and confirmed for both cases. These results, however, are not included to keep the presentation compact and focus on the main findings.

5.1. L-shaped specimen test

An L-shaped concrete panel has been considered first. A displacement is progressively applied on the panel in the vertical upward direction, see Figure 7(a). The velocity $v_0 = 740\,\mathrm{mm/s}$. The loading area is rectangular with a 30 mm diameter at the right bottom of the specimen, shown in Figure 7(a). The centre of the load is 30 mm away from the right edge. The left bottom edge is fixed. To impose the Dirichlet boundary condition for Powell-Sabin triangles, the algorithm of Ref. [30] has been employed. Test results as well as results from a numerical simulation been reported in [39]. The material parameters for the concrete are: Youngs modulus $E = 32.2$ GPa, Poissons ratio $\nu = 0.18$, density $\rho = 2210\,\mathrm{kg/m^3}$, tensile strength $t_u = 3.12$ MPa and fracture energy $\mathcal{G}_c = 58.56$ N/m. The Rayleigh wave speed is $2250\,\mathrm{m/s}$. Here, we only consider mode-I fracture, i.e. $d_{\text{int}} = 0$ in Equation (3). Plane-stress conditions have been assumed and the thickness of the panel is $h = 50$ mm. The time increment is $\Delta t = 1.0 \times 10^{-6}$s.

Copyright © 2018 John Wiley & Sons, Ltd.
Prepared using nmeauth.cls

DOI: 10.1002/nme

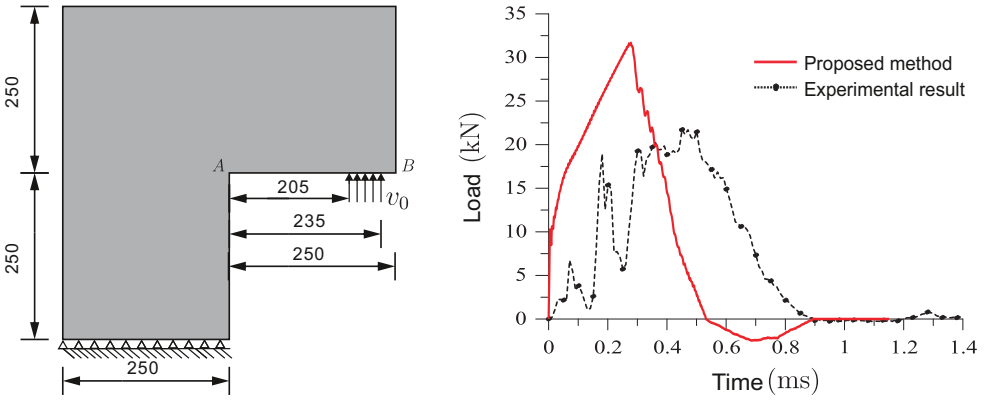

(a) geometry (in mm) and boundary conditions (b) load-time history for $v_o = 740\text{mm/s}$

Figure 7. L-shaped beam subjected to a vertical impulsive loading

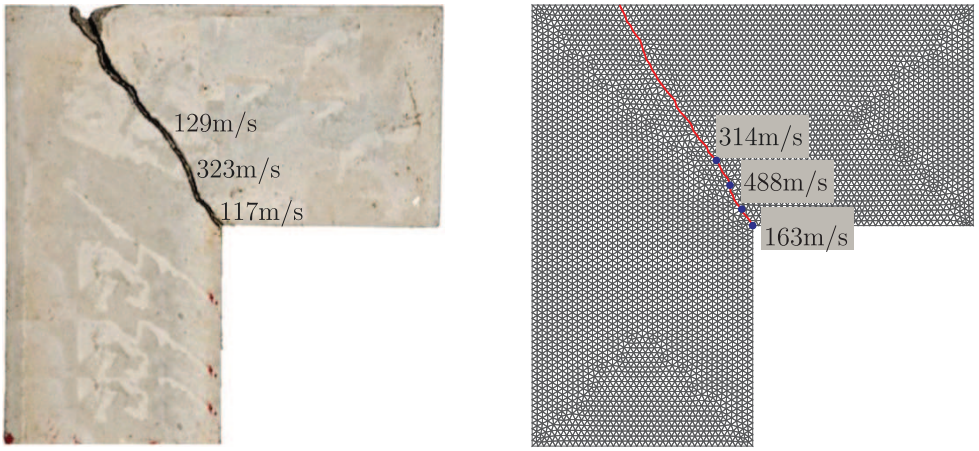

Figure 8. Experimental (left) and numerical (right) crack path and crack propagation speed. The red line in the numerical simulation indicates the crack path. The crack propagation speed has been evaluated as the average speed between two blue points $\dot{u}_a = \Delta l/\Delta t$.

The experimental result on the left of Figure 8 shows that a single crack initiates at the inner corner and propagates diagonally in an almost straight line. This corresponds to a classical mode-I crack opening. The computed crack path is presented in the right part of Figure 8. It well matches the experimental result. Figure 8 also gives the crack propagation speed, which indicates that the numerical results overestimate the experimentally observed propagation speeds. Unfortunately, Ref. [39] does not give details on how the crack propagation speed was measured and therefore, firm conclusions cannot be drawn, and neither can possible explanations be given.

The load-time history is shown in Figure 7(b). There is a similarity between the numerical and the experimental curves up to the peak load, but in the softening regime the results are different. This is probably due to the uncertainty in the test and the setup of the boundary condition in the numerical simulation. In the experiment, the bottom is constrained up to a height of 100 mm, while in the numerical simulation only the boundary itself is fixed.

Snapshots of the stress distribution and the deformed mesh are shown in Figure 9. The crack propagates gradually upon an increase of the vertical displacement. In the figure, smooth stress fields are observed as a consequence of the $\mathcal{C}^1$-continuity of the triangular elements. Stress wave reflections are observed at the boundary of the domain. Around the crack tip, interference and diffraction of the stress wave can be clearly recognised, see Figure 9.

Copyright © 2018 John Wiley & Sons, Ltd.
Prepared using nmeauth.cls

DOI: 10.1002/nme

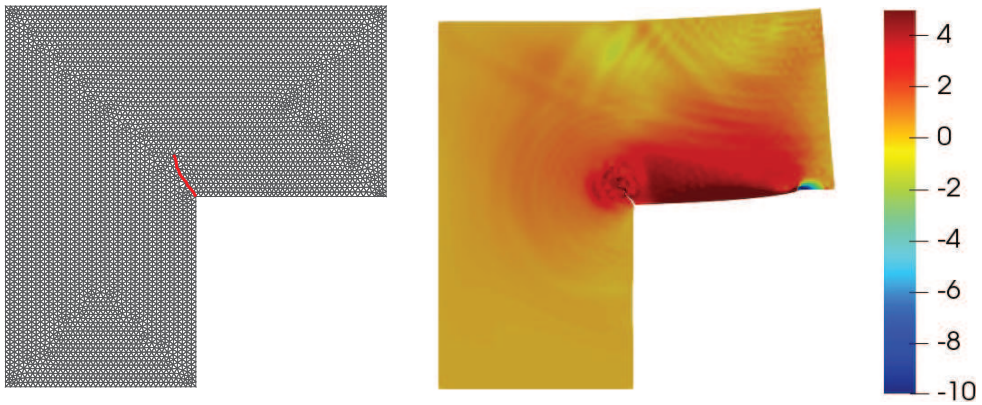

(a) mesh at time $t = 0.292$ms (b) σ_1 contour plot at time $t = 0.292$ms

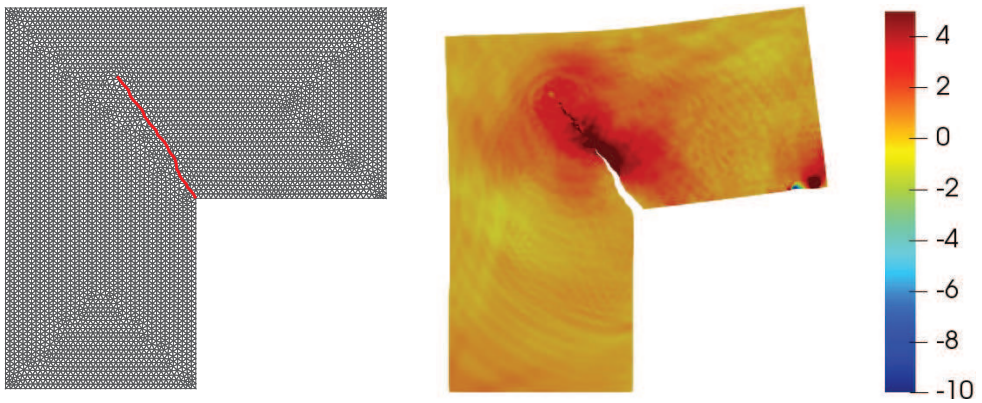

(c) mesh at time $t = 0.424$ms (b) σ_1 contour plot at time $t = 0.424$ms

Figure 9. σ_1 contours at different times. In (a) and (c), the red lines indicate the crack path. In (b) and (d), the displacements have been amplified by a factor 200.

5.2. *Edge-cracked plate under impulsive loading*

An edge-cracked panel is considered next. An impulsive load is applied to the panel [40], see Figure 10(a). The specimen is 100 mm $\times$ 200 mm and has an initial crack with length 50 mm. Due to symmetry, only half of the specimen has been considered with symmetry-enforcing boundary conditions, see Figure 10(b). The material properties are as follows: Young's modulus $E = 190$ GPa, Poisson's ratio $\nu = 0.3$, tensile strength $t_u = 1$ GPa, fracture energy $\mathcal{G}_c = 22$ kN/m and density $\rho = 8000$ kg/m^3. The Rayleigh wave speed is 2800 m/s. In this case mode-II behaviour has been considered, with $d_{\text{int}} = 1000$ N/mm and $h_s = 0$, Equation (3). Plane-strain conditions have been assumed. The specimen is loaded by an impact velocity v_0 at the bottom left edge, with a maximum value $v_0 = 16.5$m/s. The rise time is taken as $t_i = 1.0 \times 10^{-7}$s [4]. The time increment is $\Delta t = 1.0 \times 10^{-9}$s.

The computed crack path shown in Figure 11(a) is almost straight. Initially, the crack propagates at an angle of around 67° and the average angle of the crack path is about 62°, which approximately 8° smaller than the angle of 70° which has been observed experimentally [40]. The propagation speed of the crack tip is given in Figure 11(b) and is on average 65% of the Rayleigh wave speed, noting that in cohesive crack analyses the exact position of the crack tip is somewhat ambiguous. The findings are not different from results reported using the extended finite element method [4, 8]. Figure 12 gives contour plots of the principal stress σ_1 at two different times. Again, smooth stress fields are obtained due to the $\mathcal{C}^1$ continuity of Powell-Sabin B-splines. The crack propagates smoothly and no stress oscillations are observed. The reflection of the stress wave at the domain

Copyright © 2018 John Wiley & Sons, Ltd.
Prepared using nmeauth.cls

DOI: 10.1002/nme

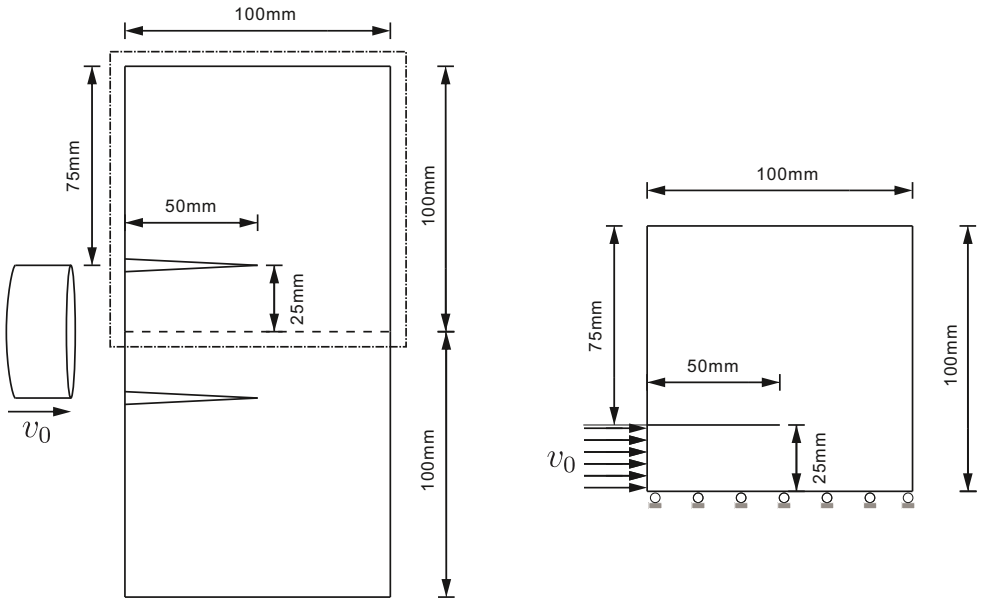

(a) geometry and boundary conditions (b) symmetrised domain for the analysis

Figure 10. Edge-cracked plate subjected to an impulsive loading

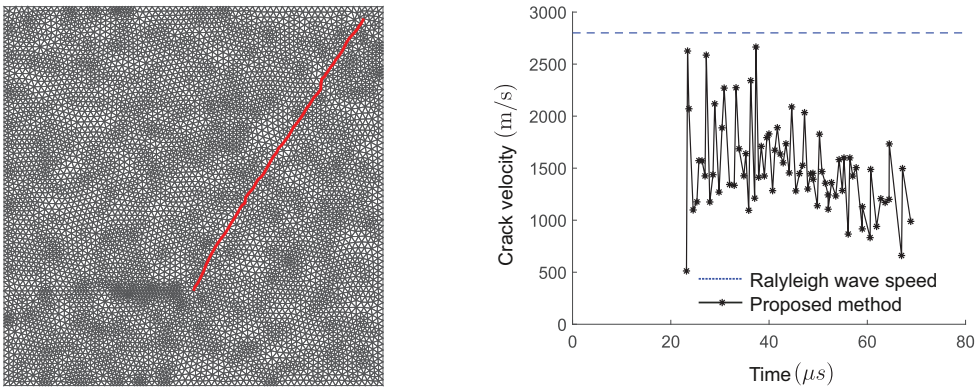

(a) predicted crack path (b) crack propagation speed

Figure 11. Simulated crack path and crack propagation speed. In (a), the red lines indicate the crack path.

boundary nicely comes out and also the interference and the diffraction of the stress wave around the crack tip are clearly visible.

6. CONCLUSIONS

Powell-Sabin B-splines have been used for the analysis of dynamic crack propagation. Powell-Sabin B-splines are based on triangles and are $\mathcal{C}^1$ continuous with respect to the interpolation of the displacement field, also across element boundaries. This implies that the stress field is continuous, again also across element boundaries. For the analysis of crack propagation Powell-Sabin B-splines have yet another important advantage, namely that the $\mathcal{C}^1$ continuity in the displacement field is preserved at crack tips, unlike for NURBS or T-splines, where the higher-order continuity breaks down at the crack tip. The preservation of the $\mathcal{C}^1$ continuity enables a direct assessment of crack initiation at the crack tip, and, in principle, by-passes the need for stress averaging over a finite

Copyright © 2018 John Wiley & Sons, Ltd.
Prepared using nmeauth.cls

DOI: 10.1002/nme

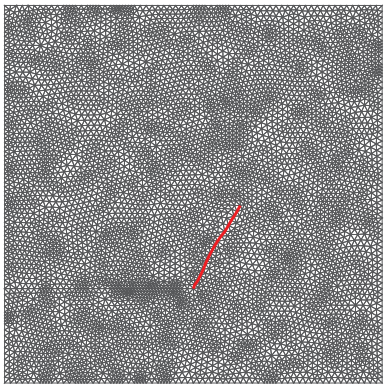

(a) mesh at time $t = 36.27\mu s$

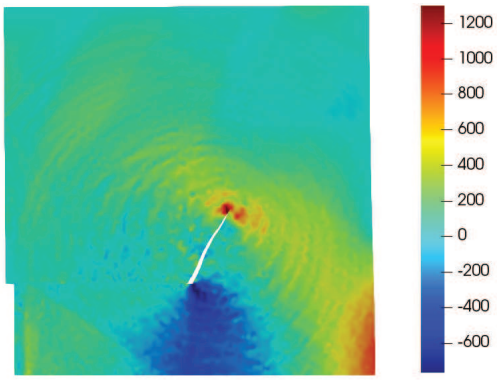

(b) σ_1 contour plot at time $t = 36.27\mu s$

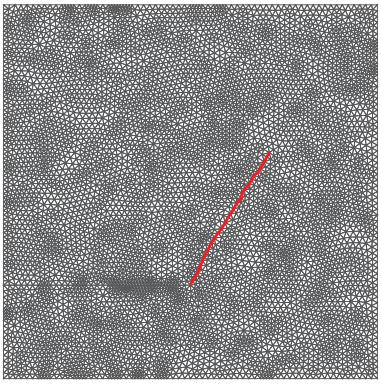

(c) mesh at time $t = 41.69\mu s$

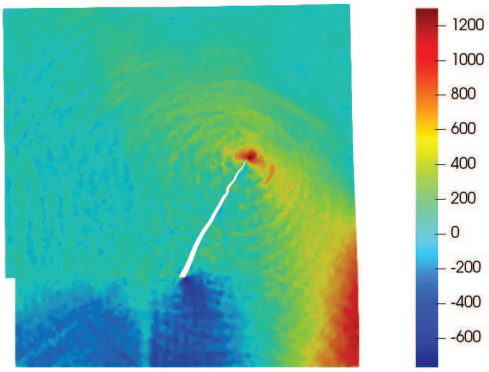

(b) σ_1 contour plot at time $t = 41.69\mu s$

Figure 12. Mesh and σ_1 contour plot at different times. In Figures (a) and (c), the red lines indicate the crack path. In Figures (b) and (d), the displacements are amplified by a factor 5.

domain around crack tips [10]. Yet, the use of such an averaging procedure was still found to be beneficial, in particular with respect to the direction of crack propagation.

Moreover, remeshing is straightforward for ($\mathcal{C}^1$-continuous) triangular elements, since standard meshing procedures can be exploited. In the process of crack propagation, the crack is introduced directly in the physical domain, which provides flexibility, and is different from procedures used for NURBS or T-splines [18, 23, 24]. After remeshing the part of the domain around the crack tip Powell-Sabin B-spline functions are introduced on the new triangles, and state vectors computed at the previous time step have to be transferred to provide initial values for next time step. The state vector mapping has been done using a novel approach in a least square setting with energy conservation acting as a constraint. This approach has been shown to be very accurate, bringing errors in the energy during the transfer process from several percents down to computed zeros. In addition, energy conservation improves the convergence behaviour of the equilibrium finding process. Indeed, due to the accumulated errors, divergence of the Newton-Raphson procedure can occur when energy conservation is not properly satisfied.

Numerical cases studies for an L-shaped specimen and an edge-cracked plate yielded fair results in terms of energy transfer, predicted crack paths and crack propagation speeds. The results for the stress fields are particularly nice, since reflection, interference and diffraction of the stress waves come out very well by virtue of the continuity of the stress fields.

Crack branching has not been addressed in the current study due to lack of proper bifurcation criteria in discrete crack models. A possibility for simulating crack branching is to insert interface elements along the boundaries of each element [3].

Copyright © 2018 John Wiley & Sons, Ltd.
Prepared using nmeauth.cls

DOI: 10.1002/nme

ACKNOWLEDGEMENT

Financial support from the European Research Council (Advanced Grant 664734 "PoroFrac") is gratefully acknowledged.

REFERENCES

[1] Xu XP, Needleman A. Void nucleation by inclusion debonding in a crystal matrix. *Modelling and Simulation in Materials Science and Engineering* 1993; **1**:111–132.

[2] Xu XP, Needleman A. Numerical simulations of fast crack growth in brittle solids. *Journal of the Mechanics and Physics of Solids* 1994; **42**:1397–1434.

[3] Camacho GT, Ortiz M. Computational modelling of impact damage in brittle materials. *International Journal of Solids and Structures* 1996; **33**:2899–2938.

[4] Remmers JJC, de Borst R, Needleman A. The simulation of dynamic crack propagation using the cohesive segments method. *Journal of the Mechanics and Physics of Solids* 2008; **56**:70–92.

[5] Papoulia KD, Vavasis SA, Ganguly P. Spatial convergence of crack nucleation using a cohesive finite-element model on a pinwheel-based mesh. *International Journal for Numerical Methods in Engineering* 2006; **67**:1–16.

[6] de Borst R, Crisfield MA, Remmers JJC, Verhoosel CV. *Non-Linear Finite Element Analysis of Solids and Structures*. Second edn., Wiley: Chichester, 2012.

[7] Belytschko T, Black T. Elastic crack growth in finite elements with minimal remeshing. *International Journal for Numerical Methods in Engineering* 1999; **45**:601–620.

[8] Belytschko T, Chen H, Xu J, Zi G. Dynamic crack propagation based on loss of hyperbolicity and a new discontinuous enrichment. *International Journal for Numerical Methods in Engineering* 2003; **58**:1873–1905.

[9] Fries TP, Belytschko T. The extended/generalized finite element method: An overview of the method and its applications. *International Journal for Numerical Methods in Engineering* 2010; **84**:253–304.

[10] Wells GN, Sluys LJ. A new method for modelling cohesive cracks using finite elements. *International Journal for Numerical Methods in Engineering* 2001; **50**:2667–2682.

[11] Xiao QZ, Karihaloo BL. Improving the accuracy of XFEM crack tip fields using higher order quadrature and statically admissible stress recovery. *International Journal for Numerical Methods in Engineering* 2006; **66**:1378–1410.

[12] Rabczuk T, Belytschko T. Cracking particles: a simplified meshfree method for arbitrary evolving cracks. *International Journal for Numerical Methods in Engineering* 2004; **61**:2316–2343.

[13] Song JH, Areias PMA, Belytschko T. A method for dynamic crack and shear band propagation with phantom nodes. *International Journal for Numerical Methods in Engineering* 2006; **67**:868–893.

[14] Li B, Peco C, Millán D, Arias I, Arroyo M. Phase-field modeling and simulation of fracture in brittle materials with strongly anisotropic surface energy. *International Journal for Numerical Methods in Engineering* 2015; **102**(3-4):711–727.

[15] de Borst R, Verhoosel CV. Gradient damage vs phase-field approaches for fracture: Similarities and differences. *Computer Methods in Applied Mechanics and Engineering* 2016; **312**:78–94.

[16] Li B, Maurini C. Crack kinking in a variational phase-field model of brittle fracture with strongly anisotropic surface energy. *Journal of the Mechanics and Physics of Solids* 2019; **125**:502–522.

[17] Borden MJ, Verhoosel CV, Scott MA, Hughes TJ, Landis CM. A phase-field description of dynamic brittle fracture. *Computer Methods in Applied Mechanics and Engineering* 2012; **217**:77–95.

[18] Verhoosel CV, Scott MA, de Borst R, Hughes TJR. An isogeometric approach to cohesive zone modeling. *International Journal for Numerical Methods in Engineering* 2011; **87**:336–360.

[19] Irzal F, Remmers JJC, Verhoosel CV, de Borst R. An isogeometric analysis Bézier interface element for mechanical and poromechanical fracture problems. *International Journal for Numerical Methods in Engineering* 2014; **97**:608–628.

Copyright © 2018 John Wiley & Sons, Ltd.

Prepared using nmeauth.cls
DOI: 10.1002/nme

[20] Vignollet J, May S, de Borst R. On the numerical integration of isogeometric interface elements. *International Journal for Numerical Methods in Engineering* 2015; **102**:1773–1749.

[21] Vignollet J, May S, de Borst R. Isogeometric analysis of fluid-saturated porous media including flow in the cracks. *International Journal for Numerical Methods in Engineering* 2016; **108**:990–1006.

[22] May S, de Borst R, Vignollet J. Powell-Sabin B-splines for smeared and discrete approaches to fracture in quasi-brittle materials. *Computer Methods in Applied Mechanics and Engineering* 2016; **307**:193–214.

[23] Chen L, Lingen FJ, de Borst R. Adaptive hierarchical refinement of NURBS in cohesive fracture analysis. *International Journal for Numerical Methods in Engineering* 2017; **112**:2151–2173.

[24] Chen L, Verhoosel CV, de Borst R. Discrete fracture analysis using locally refined T-splines. *International Journal for Numerical Methods in Engineering* 2018; **116**:117–140.

[25] De Luycker E, Benson DJ, Belytschko T, Bazilevs Y, Hsu MC. X-fem in isogeometric analysis for linear fracture mechanics. *International Journal for Numerical Methods in Engineering* 2011; **87**(6):541–565.

[26] Powell MJD, Sabin MA. Piecewise quadratic approximations on triangles. *ACM Transactions on Mathematical Software (TOMS)* 1977; **3**:316–325.

[27] Dierckx P, Van Leemput S, Vermeire T. Algorithms for surface fitting using Powell-Sabin splines. *IMA Journal of Numerical Analysis* 1992; **12**:271–299.

[28] Vanraes E, Windmolders J, Bultheel A, Dierckx P. Automatic construction of control triangles for subdivided Powell-Sabin splines. *Computer Aided Geometric Design* 2004; **21**:671–682.

[29] May S, Vignollet J, de Borst R. Powell-Sabin B-splines and unstructured standard T-splines for the solution of Kichhoff-Love plate theory using Bézier extraction. *International Journal for Numerical Methods in Engineering* 2016; **107**:205–233.

[30] Chen L, de Borst R. Cohesive fracture analysis using Powell-Sabin B-splines. *International Journal for Numerical and Analytical Methods in Geomechanics* 2019; **43**:625–640.

[31] Newmark NM. A method of computation for structural dynamics. *Journal of the Engineering Mechanics Division* 1959; **85**:67–94.

[32] Geuzaine C, Remacle JF. Gmsh: A 3-D finite element mesh generator with built-in pre-and post-processing facilities. *International Journal for Numerical Methods in Engineering* 2009; **79**:1309–1331.

[33] O'Rourke J, Aggarwal A, Maddila S, Baldwin M. An optimal algorithm for finding minimal enclosing triangles. *Journal of Algorithms* 1986; **7**:258–269.

[34] Amestoy M, Leblond JB. Crack paths in plane situations – II. Detailed form of the expansion of the stress intensity factors. *International Journal of Solids and Structures* 1992; **29**:465–501.

[35] Schütte H. Curved crack propagation based on configurational forces. *Computational Materials Science* 2009; **46**:642–646.

[36] Chen L, de Borst R. Locally refined T-splines. *International Journal for Numerical Methods in Engineering* 2018; **114**:637–659.

[37] Chen L, de Borst R. Adaptive refinement of hierarchical T-splines. *Computer Methods in Applied Mechanics and Engineering* 2018; **337**:220–245.

[38] de Borst R, Chen L. The role of Bézier extraction in adaptive isogeometric analysis: Local refinement and hierarchical refinement. *International Journal for Numerical Methods in Engineering* 2018; **113**:999–1019.

[39] Ožbolt J, Bede N, Sharma A, Mayer U. Dynamic fracture of concrete L-specimen: Experimental and numerical study. *Engineering Fracture Mechanics* 2015; **148**:27–41.

[40] Kalthoff JK, Winkler S. Failure mode transition at high rates of loading. *Proceedings of the International Conference on Impact Loading and Dynamic Behavior of Materials*, 1988; 43–56.

[41] Worsey AJ, Piper B. A trivariate Powell-Sabin interpolant. *Computer Aided Geometric Design* 1988; **5**:177–186.

[42] Sorokina T, Worsey AJ. A multivariate Powell-Sabin interpolant. *Advances in Computational Mathematics* 2008; **29**:71–89.

Copyright © 2018 John Wiley & Sons, Ltd.
Prepared using nmeauth.cls

DOI: 10.1002/nme